CONF-870812--27

DE87 011466

TEMP-STRESS analysis of a reinforced concrete vessel under internal pressure.*

A. H. Marchertas, J. M. Kennedy, and P. A. Pfeiffer, Argonne National Laboratory, Argonne, Illinois 60439-4842.

1 INTRODUCTION

Prediction of the response of the Sandia National Laboratory 1/6-scale reinforced concrete containment model test shown in Fig. 1 was obtained by Argonne National Laboratory (ANL) employing a computer program developed by ANL. The test model is to be internally pressurized to failure. The two-dimensional code TEMP-STRESS [1-5] has been developed at ANL for stress analysis of plane and axisymmetric 2-D reinforced structures under various thermal conditions. The program is applicable to a wide variety of nonlinear problems, and is utilized in the present study. The comparison of these pretest computations with test data on the containment model should be a good indication of the state of the code.

2 ANALYTICAL APPROACH

The analytical approach in TEMP-STRESS is based on the explicit temporal integration coupled with dynamic relaxation. This enables the code to be used for static as well as dynamic problems. The choice of the integration scheme was primarily dictated by the highly nonlinear concrete behavior and the relative ease of accounting for nonlinearity in this type of algorithm, and the fact that, although within each load step this procedure introduces some dynamic response, iteration to equilibrium is always possible. Equilibrium of the system is checked by means of two criteria. One criterion makes a comparison of the unbalanced force with the internal force, while in the other criterion, the displacements are compared at successive iteration steps.

---

*This work was performed under the auspices of the U. S. Department of Energy, Office of Technology Support Program, under contract W-31-109-Eng-38.

2.1 TEMP-STRESS simulation

TEMP-STRESS is a 2-D code for the stress analysis of plane and axisymmetric reinforced/prestressed concrete problems. Elements available for representing the materials are a quadrilateral continuum element with one-point integration and a flexural element with two-point integration along its length and an arbitrary number of integration points through the depth. Both of these elements can model the direction, the position, and the percentage of reinforcements. The rebars are assumed to remain rigidly bonded to the concrete; debonding of rebars and concrete is not considered.

Reinforcement in the continuum element can be specified in the hoop direction and arbitrary orthogonal directions in the r-z or the x-y plane. In the flexural element, reinforcement can be specified at arbitrary layers measured from the neutral axis and spanning from the axial (meridional) direction through the hoop direction. Inclined reinforcement through the depth of the cross-section, representing the connecting ties, can also be treated. The simulation of cracking in the elements is defined at the integration points. Thus, a total of three orthogonal cracks may coexist at the centroid of the axisymmetric continuum element: one crack in the hoop direction and two orthogonal cracks in the r-z plane. Similarly, two orthogonal cracks may occur in the axisymmetric shell element at each Gaussian integration point: one crack in the hoop direction and one crack in the meridional direction.

In addition to that specified within the concrete elements, reinforcement can also be modeled by means of discrete rod and ring elements. A combination of all these elements was used to represent the details of reinforcement in the containment test structure.

The strength capacity of the concrete in multiaxial stress space is characterized by the so-called Hsieh-Ting-Chen [6] four parameter failure surface. The concrete response after failure is simulated using the element-size-independent cracking criterion established by Bazant and Oh [7]. In the uniaxial stress-strain relationship, a linear reduction of strength is specified from the ultimate stress down to zero. The maximum strain in tension (where the stress is specified as zero) for the solutions described in this paper is 0.0007.

2.2 Material models

Both steel and concrete were modeled as nonlinear materials. The constitutive equations for these materials are based on an elastic-plastic law with initial yielding and the subsequent loading surface described by the von Mises condition. An associated flow rule is used.

The properties of the concrete are: Young's modulus = 4800 ksi (33.1 GPa), Poisson's ratio = 0.2, compression strength = 6800 psi (46.9 MPa) and tensile strength = 500 psi (3.45 MPa). Properties of the rebar are: Young's modulus = 31000 ksi (214 GPa), Poisson's ratio = 0.3, yield stress = 66.6 ksi (459 MPa) and ultimate stress = 99 ksi (683 MPa) at 4.62% strain. Also, the liner properties are: Young's modulus = 30000 ksi (207 GPa), Poisson's ratio = 0.3, yield stress = 50.2 ksi (346 MPa) and ultimate stress = 70 ksi (483 MPa) at 16.4% strain. The rebar material properties were modified to take

into account the strength of the splices. Wherever mechanical splices are located, there, the strength of the rebar is assumed to be the average holding strength of the splice. The average strength capacity of the splice is considered to be 99 ksi (683 MPa).

3 FINITE ELEMENT MODEL

The finite element models, which are utilized to predict the response of the test structure under internal pressurization, vary in complexity. This finite element model consists only of the axisymmetric cylindrical vessel and a spherical dome. The purpose of this simplified reinforced shell model, which is composed only of axisymmetric reinforced shell elements, is to portray the global response of the vessel. It is shown in Fig. 2. This model consists of 31 reinforced concrete shell elements: 11 of them representing the 7 in. (17.78 cm) thick spherical dome, one element representing the transition from the dome to the cylinder, and 18 elements representing the 9 3/4 in. (24.77 cm) thick cylinder. A liner on the inside surface of the vessel is made up of steel elements. The liner elements, which are offset from the concrete elements, have different thicknesses: 0.09 in. (0.229 cm) in the dome and 0.068 in. (0.173 cm) in the cylinder.

The modeling of the reinforcement closely corresponds to the structural specifications of the containment structure. The number of reinforcement layers ranges from four in the spherical dome to 10 layers at the base of the cylinder. Fourteen different combinations of reinforcements are used within the flexural elements.

This model provides information on the response of the containment vessel relative to the vertical displacement of the cylinder base. Deformation of the vessel, as well as the strains in the liner and the rebars are obtained for internal pressures ranging from 5 psi (0.0345 MPa) up to 160 psi (1.103 MPa). Maximum vertical displacement at the dome apex before impending failure of the hoop splices is 1.9 in. (4.8 cm), the corresponding vertical and horizontal displacements at the vessel spring line are 2.2 in. (5.6 cm) and 1.9 in. (4.8 cm). The maximum radial deformation at mid-height of the cylinder at the same instant is 5.3 in. (13.5 cm) and the respective strain in the liner is 0.04.

Pressurization of the shell model is accomplished by monotonically increasing the internal loading in 5 psi (0.0345 MPa) increments, after an initial pressure increment of 5 psi (0.0345 MPa). The important milestones of the general response of the shell model are shown in Table 1. It is observed that up to 25 psi (0.172 MPa) the behavior of the vessel is entirely elastic. At internal pressures 25-40 psi (0.172 - 0.276 MPa) meridional cracking at the base of the vessel propagates from the inside of the vessel to the neutral surface. The onset of hoop and meridional cracking in the cylinder above 40 psi (0.276 MPa) is followed by hoop and meridional cracking in the dome. Hoop cracking is practically completed at 90 psi (0.621 MPa) and 115 psi (0.793 MPa).

Yielding of the liner is observed at about 85 psi (0.586 MPa) and spreads along the cylinder - and, reaches the base at about 95 psi (0.655 MPa). The yielding of hoop reinforcement on the inside of the concrete vessel begins at about 100-105 psi (0.689 - 0.724 MPa).

Failure of hoop reinforcement is governed by the strength of the splices; the ultimate stress of 99 ksi (683 MPa) is reached at the internal pressure of 155-160 psi (1.069 - 1.103 MPa). Failure of the hoop reinforcement in turn causes the liner to rupture. The deformed configuration of the vessel, before impending failure, is shown in Fig. 3.

Table 1. Sequence of Shell Response to Pressurization

Pressure		Response
psi	MPa	
0 - 25	0-0.172	Elastic behavior.
25 - 40	0.172-0.276	Meridional cracking on inside base of vessel.
40 - 90	0.276-0.621	Hoop cracking in cylinder and hoop/meridional cracking of the dome.
40 -115	0.276-0.793	Meridional cracking in the cylinder.
85 - 95	0.586-0.655	Yielding of liner begins and spreads along cylinder.
90 - 95	0.621-0.655	Yielding of liner at the base.
100 - 105	0.689-0.724	Yielding of hoop reinforcement starts.
155 - 160	1.069-1.103	The ultimate strength of the splice is reached in the cylinder (at point A in Fig. 3) leading to failure of the liner.

4 CONCLUSIONS

The TEMP-STRESS finite element model described in this paper represents an axisymmetric simulation of the reinforced concrete vessel to internal pressurization. The information derived shows the global deformation, the state of strain/stress within the containment vessel with respect to the imposed pressures. Thus, the location and progress of concrete cracking, the stretching of the liner and the reinforcing bars and final failure are indicated through the entire loading range. Equilibrium of the entire system is assured at definite loading increments.

It is shown by the analytical model that with the progress of concrete cracking, the resisting load is continuously transferred to

the reinforcing bars and the liner. Thus, after the tensile strength is exceeded and the concrete stress is set to zero, the internal pressures are entirely resisted by the liner and the reserve strength of the reinforcing bars. The reinforcing bars are mechanically connected to each other by splices, the ultimate strength of which is less than that of the rebars themselves. The corresponding strain at this limiting stress is lower than the ultimate strain of the liner. Therefore, the specified ultimate strength of the splices limits the pressurization of the vessel. Furthermore, once any of the splices fail, then load is transferred to the adjacent members, causing their failure and general failure of the vessel.

The axisymmetric model provides only information on the global response of the structure. Such is also the prediction of failure. In fact, however, failure of the reinforced concrete containment structure would most likely initiate at a local stress concentration, in the liner. Progressive rupture of the liner could then result to the extent of causing excessive leakage.

One possible area of failure is the junction of the cylinder wall to the base. It seems probable that weld failure could occur here and thus initiate the failure of liner. Another possibility would be local stress concentrations in the penetrations through the walls of the vessel. Both of these concerns could be further investigated by three-dimensional models.

References

1. Marchertas, A. H., & R. F. Kulak 1981. "Numerical Modeling of Concrete Under Thermal Loads," Nuclear Engineering and Design, 68 (2), 225-236.

2. Marchertas, A. H., & R. F. Kulak 1982. "A Coupled Heat Conduction and Thermal Stress Formulation Using Explicit Integration," ANL-82/47.

3. Marchertas, A. H., & R. F. Kulak 1982. "Response Simulation of Concrete Structures to High Temperatures," Proc. of the Workshop on Containment Integrity, W. A. Sebrell (ed.), Vol. 1, NUREG/CP-0033, SAND82-1659.

4. Takahashi, Y., 1983. "Elastic-Plastic Constitutive Modeling of Concrete," ANL-83/23.

5. Marchertas, A. H., 1984. "Thermo-Mechanical Analysis of Concrete in LMRBR Programs," Nuclear Engineering and Design, 82 (1), 47-62.

6. Hsieh, S. S., E. C. Ting & W. F. Chen 1982. "A Plastic-Fracture Model for Concrete," Int. J. Solids Structures, 18 (3), pp. 181-197.

7. Bazant, Z. P., & B. H. Oh "Crack Band Theory for Fracture of Concrete," Materiaux et Constructions, 16, (93), 155-177.

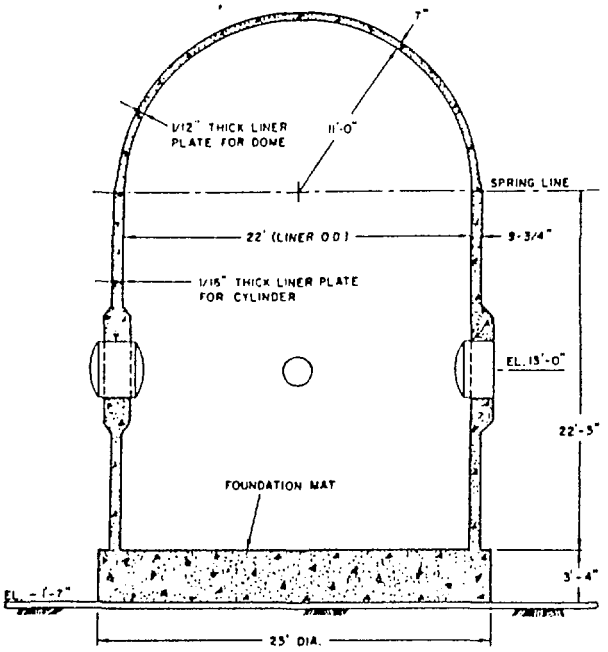

Figure 1. Reinforced Concrete Containment

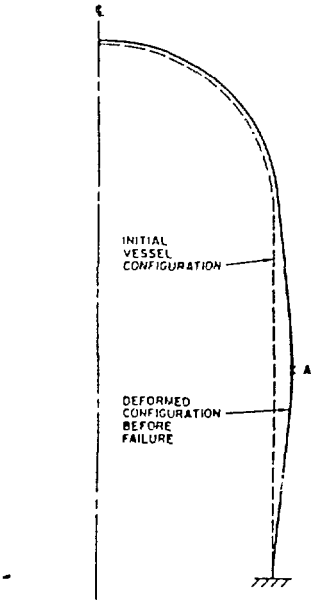

Figure 3. Vessel Deformation at Impending Failure

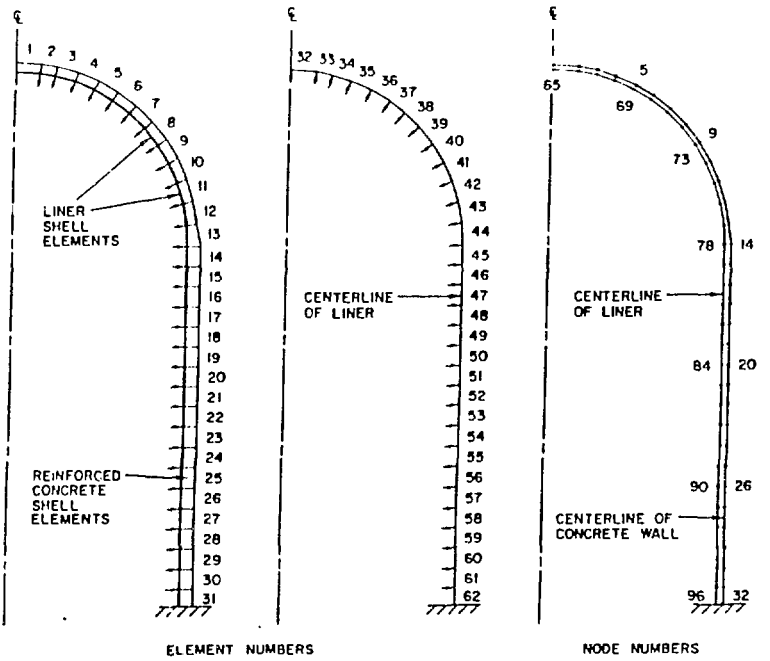

Figure 2. Discretization of Containment Model

CONF-870816--27

Paper submitted for presentation to the 24th ASME/AIChE National Heat Transfer Conference, Pittsburgh, PA, August 9-12, 1987.

INVESTIGATION OF MOLTEN CORIUM-CONCRETE INTERACTION PHENOMENA AND AEROSOL RELEASE*

by

B. W. Spencer, D. H. Thompson, D. R. Armstrong, J. K. Fink, W. H. Gunther, and D. J. Kilsdonk

Reactor Analysis and Safety Division
Argonne National Laboratory
9700 South Cass Avenue
Argonne, IL 60439

CONF-870816--27

DE87 011407

and

B. R. Sehgal

Electric Power Research Institute
3412 Hillview Avenue
Palo Alto, CA 94303

*Work sponsored by the Electric Power Research Institute, Palo Alto, CA.

INVESTIGATION OF MOLTEN CORIUM-CONCRETE INTERACTION PHENOMENA AND AEROSOL RELEASE

by

B. W. Spencer, D. H. Thompson, D. R. Armstrong, J. K. Fink,
W. H. Gunther, and D. J. Kilsdonk (ANL)

and

B. R. Sehgal (EPRI)

ABSTRACT

The Electric Power Research Institute is sponsoring a program of laboratory investigations at Argonne National Laboratory to study the interaction between molten core materials and reactor concrete basemats during postulated severe reactor accidents, with particular emphasis on measurements of the magnitude and chemical species present in the aerosol releases. The approach in this program is to sustain internal heat generation in reactor-material corium using direct electrical heating and to develop test operating and diagnostics capabilities with a series of small- and intermediate-scale scoping tests followed by fully instrumented large-scale testing. Real reactor materials (UO_2, ZrO_2, oxides of stainless steel, plus metallics) are used, with small amounts of La_2O_3, BaO, and SrO added to simulate nonvolatile fission products. In intermediate-scale scoping tests completed to date, corium inventories of up to 29 kg have been heated with power inputs in excess of 1 kW/kg melt. The measured concrete ablation rates have ranged from 0.9 to 3.9 mm/minute. Aerosol samples have been examined using a scanning electron microscope and show submicron particles, 2-6 micrometer spheres, and agglomerates that range from a few micrometers to strings 13 micrometers in length.

INTRODUCTION

Background

The risk posed by a postulated severe accident in an LWR system is under extensive investigation by the NRC and its contractors and by various industry groups.[1,2] This risk is dominated by accident sequences in which it is assumed that there are one or more postulated initiating faults, the diverse and redundant plant protection and safety systems are simultaneously assumed to be inoperable, and there is no recovery of these systems through the time that dose-significant amounts of radioactive materials are released from the plant. Although the likelihood of such a severe accident is acknowledged to be extremely small, there is nonetheless extensive research under way examining the release of radioactive materials from the fuel to the containment atmosphere during these postulated core melt sequences.

The accident progression begins with an in-vessel stage involving core uncovery, heatup of core materials, cladding oxidation by steam, liquifaction of core materials, and downward relocation of molten materials (now denoted as corium) into the vessel lower head. Without recovery of safety systems, the corium will eventually penetrate the lower head and flow into the reactor cavity or pedestal region below. The initial ex-vessel events are largely determined by two sequence-dependent parameters, namely: 1) the vessel-to-containment pressure difference which determines the vigorousness of both the corium ejection as well as the ensuing vessel blowdown, and 2) the possible presence of a sufficient water mass in the cavity region to cause even a partial quench of the molten core material. A vessel-to-containment pressure difference of a few hundred psi or greater will likely

disperse much of the corium from the cavity to other parts of the containment due to entrainment and sweepout with the steam/hydrogen mixture from vessel blowdown.[3] Assuming the containment withstands any possible liner ablation or atmosphere heatup accompanying the dispersal, the debris would likely be spread out over large surface areas with relatively small layer thicknesses such that its temperature would be too low for any significant interaction with the concrete.

In the molten-core/concrete interaction (MCCI) studies, attention is focused on those sequences in which the corium largely remains in the reactor cavity or pedestal region following failure of the vessel head. In this case, the corium layer thickness is of sufficient depth that high corium temperatures can be sustained from internal heat generation (plus exothermic oxidation) causing the concrete to decompose and melt, releasing large quantities of steam and CO_2. The presence of water in the cavity may delay this process if there is a significant quenching of the corium. However, the water will simply boil off in time unless a reflux cycle is established in the containment. It remains to be determined what the long-term effect of overlying water is with regard to mitigating concrete erosion given that a reflux cycle can be established. At minimum, there would be appreciable benefit of the presence of a water layer in lessening the vapor and aerosol release from the core-concrete interaction.

Interaction of corium with concrete at the bottom of the reactor cavity takes place in four stages, namely:

Stage 1 - Corium Jet Impingement

The corium flows from the bottom of the failed reactor pressure vessel (RPV) and impinges on the concrete base, splashing and spreading out on the

base. The basemat is rapidly eroded by the impingement heat flux, but the duration of the jet impingement is relatively short. An aerosol "spike" is expected at this time. The corium temperature may be reduced initially by partial quenching if water is present in the cavity. The corium temperature will be additionally reduced due to the impingement heat flux into the concrete and the heat sink provided by the concrete decomposition products mixing with the corium.[4] Hence, the initial conditions of the MCCI are influenced by heat losses and dilution of the melt which occurs during the impingement stage.

Stage 2 - Early Aggressive Interaction Stage

Oxidation of metallic species in the corium, notably zirconium, is a major contributor to the internal heat generation during this stage. The corium is spread to a nominally uniform depth on the available floor area in the cavity. The lateral dimension of the cavity is typically much larger than the depth of the corium layer, and hence the MCCI is well characterized as a one-dimensional process. The chemical energy plus decay heat are lost from the melt layer by heat transfer processes which typically involve a downward flux into the basemat concrete, an upward loss by radiation and convection to the overlying atmosphere and structure, and an upward loss by transport of the gases flowing though the melt layer. The early aggressive interaction stage is characterized by relatively high melt temperature, relatively rapid downward erosion of the concrete, high gas flow through the melt layer from decomposition of the concrete, boilup of the melt layer and possibly good mixing of the melt constituents due to the high gas flow, and releases of aerosol and fission products.

Stage 3 - Long-term Erosion Stage

Oxidation of metallic species will eventually become complete, and internal heat generation will take place by decay heating only. The fully oxide melt has been considerably diluted by concrete decomposition products by this time. The corium temperature is much lower, but the corium solidus has been reduced by addition of the concrete decomposition products. The concrete erosion continues at a reduced rate, and the slower gas release produces a bubbly flow regime. The aerosol and fission-product release is small, but continues for a long period of time.

Stage 4 - Solidification Stage

The temperature of the melt eventually reduces to the corium solidus and thick crust zones are formed. Downward penetration occurs at an exceedingly slow rate. Aerosol generation becomes negligible.

Objectives

The overall objectives of the research program are to add to the data base involving reactor-material experiments for both the thermal hydraulics as well as aerosol and fission product release aspects of MCCI, and to evaluate predictions of key modeling/code development efforts in light of the experiment measurements. Specifically, the objectives of the program are to obtain data for various corium and concrete compositions on phenomena that control: a) the melt-layer temperature-time history such as downward heat flux (and concrete erosion rate), gas release rate and effects, exothermic and endothermic chemical reactions, and upward heat loss, and b) the overall release rates of aerosols (particularly containing fuel and fission products) and the extent to which metallic

constituents of the corium may enhance the release of normally nonvolatile fission products through chemical reactions between the melt species and the concrete decomposition gasses. An additional objective is to compare predictions of codes such as CORCON/VANESA, various modified versions of CORCON, and DECOMP/METOXA, among others, with experiment results.

Approach

Real reactor materials are utilized in a long-term interaction with an underlying slab of concrete. Sustained internal heat generation is provided by the method of direct electrical heating (DEH) to simulate decay heat or to control the corium temperature at a prescribed quasi-static level. The tests are evolving from small scale (5 kg corium mass) to larger scale (30 and 300 kg) as the experiment technique and diagnostic tools are progressively improved. Presently, 5 kg and 30 kg size gas sparging tests have been completed and 30 kg integral MCCI tests are under way. The corium mixtures are either fully oxidized for tests applicable to the long-term erosion stage or contain metallic constituents for tests applicable to the early, aggessive interaction stage. The corium mixtures consist of UO_2, ZrO_2, stainless steel oxides, plus nonradioactive fission product mockups La_2O_3, BaO, and SrO; Zr and metallic stainless steel are added for tests involving a metallic constituent. Current tests utilize a limestone/common sand concrete of specific composition matching that used at the Zion station; future tests are also planned to examine limestone/limestone and basaltic concrete. The tests are presently one dimensional, designed to minimize (but measure) lateral heat losses such that the predominant heat transport processes are vertically upward and downward.

The experiment approach is to provide instrumentation to enable evaluations of concrete erosion rate, melt layer temperature and heat balance measurements, time variation of gas release rate and composition, and time variation of aerosol release rate and characteristics. Much of this diagnostics capability is in an evolutionary state and will continue to be upgraded as experience and needs dictate.

DESCRIPTION OF EXPERIMENT SYSTEM

The hardware for the experiment consists of the corium containment apparatus, an electric power supply, a water cooling system, a sparge/carrier gas system, an aerosol collection and gas sampling system, a ventilation and filtration system, and a data acquisition system. Included in the aerosol collection and gas sampling system are a carrier gas injector, main gas piping and filters, two sample subsystems--an array of filter and gas sample lines and an aerosol sample canister, and on-line gas analysis equipment. An isokinetic sample of the carrier- and reaction-gas stream is drawn through the filter/gas sample array and the aerosol sample canister. Gas samples are collected at different times during the MCCI for subsequent analysis.

The apparatus for intermediate-scale molten corium-concrete interaction tests is illustrated in Fig. 1. It consists of a series of "U"-shaped brass segments, electrically insulated from each other, that are stacked side by side to form the base and sides of the electrical melt generator. Tungsten electrodes, supported in machined electrical insulators, form the ends of the apparatus. The sides and ends of the apparatus are water

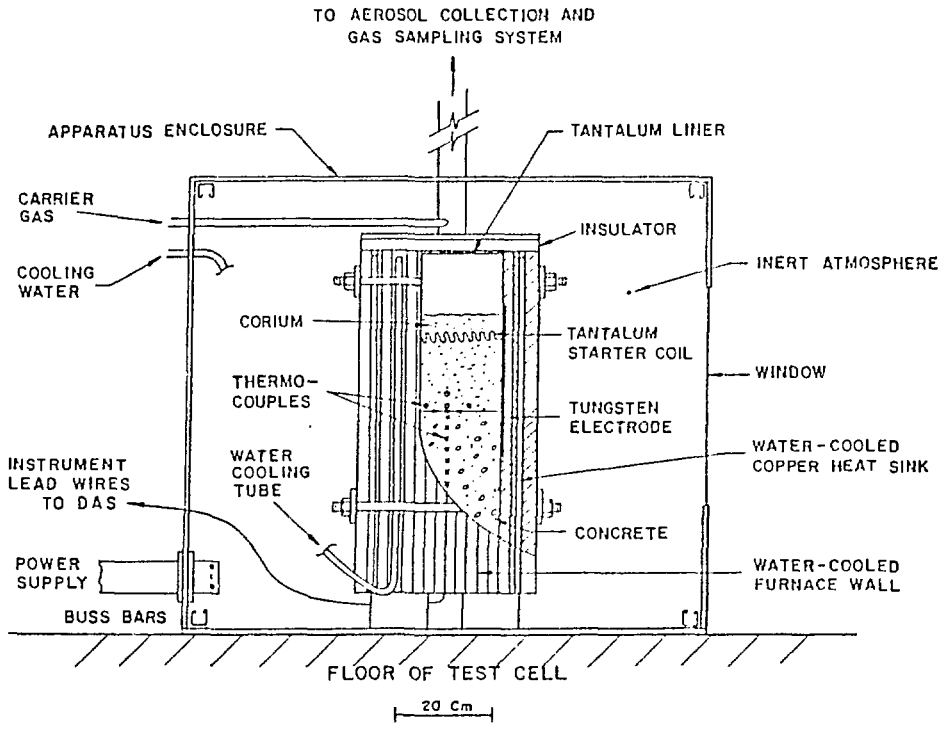

Figure 1. Illustration of Apparatus for Intermediate-Scale MCCI Tests.

cooled. Heat losses are individually monitored through each wall. A thick layer of thermal insulation rests on the top of the apparatus and supports the top cover, which is the base of the aerosol collection and gas sampling system.

The apparatus is instrumented to monitor test operation and to log data for subsequent evaluation. Parameters monitored include the input power, directional heat losses, corium temperature, sparge/carrier gas temperature and flow rate, and temperatures within the concrete basemat. Also input to the data acquisition system are gas temperatures in the aerosol collection and gas sampling system. Power for internal heat generation in the corium is provided by a power supply consisting of a high-voltage, low-current transformer for the low-power preheat and a low-voltage, high-current transformer for high-power operation.

Development of an aerosol collection and gas sampling system was begun prior to the first intermediate-scale MCCI test. A carrier gas injector was constructed to introduce an annular stream of inert gas around the off gas leaving the test cavity. This measured flow of inert gas reduces the temperature of the off gas and dilutes the aerosol concentration. The sampling system contains bottles for collecting gas samples and stainless steel coupons in the main gas stream to collect aerosol samples.

Improvements were made in the aerosol collection and gas sampling system as MCCI testing continued. The system used for MCCI test I-7 is illustrated in Fig. 2. It consists of the carrier gas injector, main flow piping and filters, a bank of five filter and gas sample lines, an aerosol sample canister similar to that used in the Source Term Experiments Projects (STEP) in-reactor tests,[5] plus CO, CO_2, and H_2O monitors.

The STEP canister contains 14 aerosol collection stages in each of three chambers. Each stage consists of a labyrinthine flow channel with settling plates and wire impactors for particle collection. Prior to the STEP in-reactor tests, the canisters were calibrated via laboratory experiments to determine the collection efficiencies of the wires and settling plates as a function of particle size. One of the 14-stage chambers in the STEP canister was used to collect aerosol samples during MCCI test I-7.

The apparatus for a MCCI test is assembled around the concrete basemat, then moved into the test cell and connected to the support systems. Blended corium powder is loaded into the test cavity atop the basemat and tamped to a density of about 3.5 g/cm^3. Thermowells and tantalum starter coils are installed at the selected elevations during the corium loading process. The composition of the test materials is shown in Table 1.

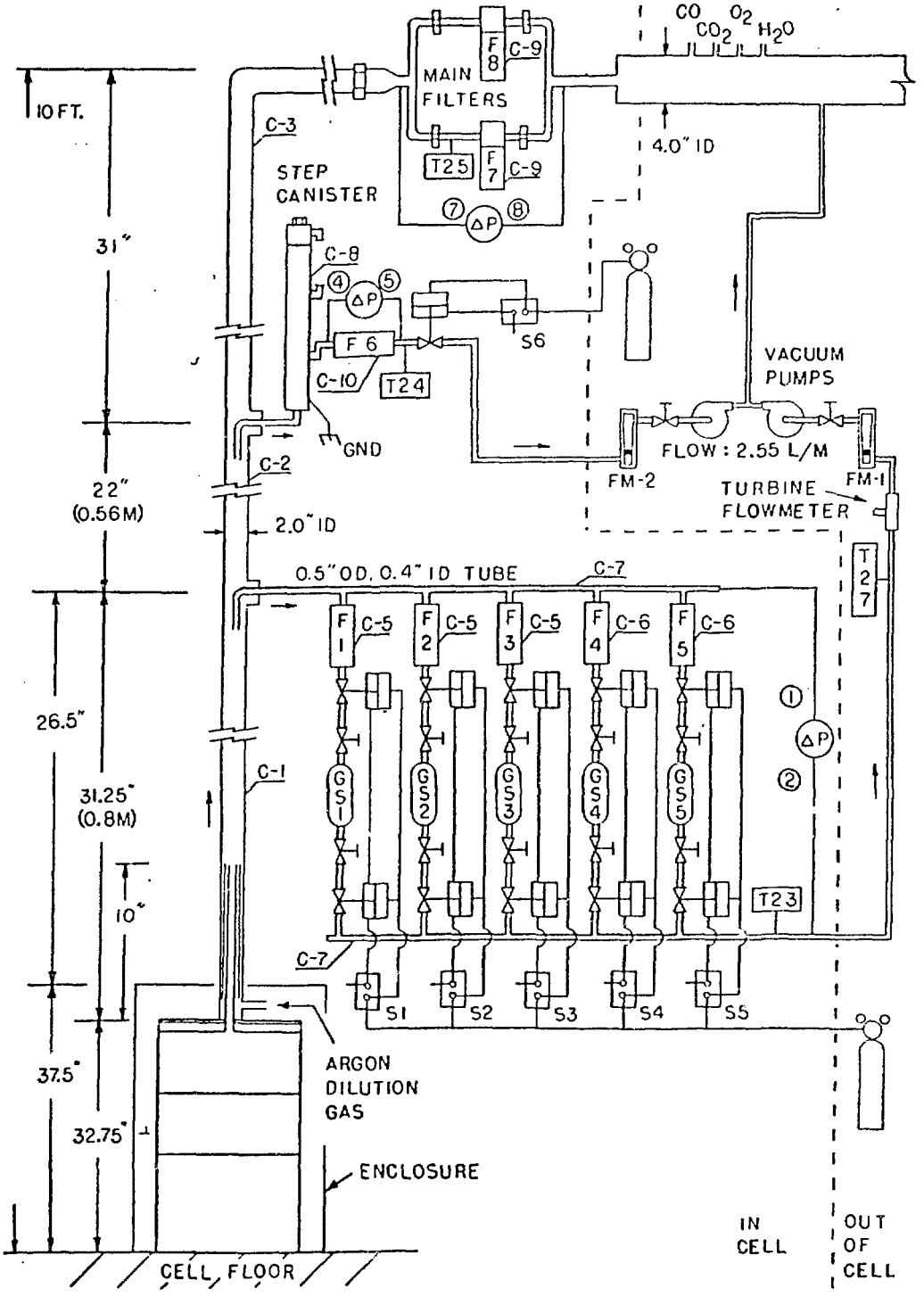

Figure 2. Schematic of Aerosol Collection and Gas Sampling System.

TABLE 1. COMPOSITION OF TEST MATERIALS

Constituent	Composition, w/o
Corium	
UO_2	54.5
ZrO_2	14.5
Cr_2O_3	5.7
NiO	2.2
Fe_2O_3	23.1
Limestone/Common Sand (Zion) Concrete	
SiO_2	38.26
TiO_2	0.04
MgO	8.16
CaO	24.12
Na_2O	0.05
K_2O	0.09
Fe_2O_3	0.77
Al_2O_3	1.72
CO_2	20.33
H_2O evap	4.22
H_2O bound	2.00
SO_3	0.24

Following installation of the top cover on the apparatus, the gas system is assembled. Both the test apparatus, apparatus enclosure, and the gas system are purged with inert gas prior to test initiation. A test is operated in the preheat mode until the corium powder increases in temperature sufficiently to become electrically conductive. This process is aided by the tantalum starter coils buried in the corium and connected to the tungsten

electrodes. After transition to the high-power mode of operation, the power input is varied through the planned test sequence. Test operation is guided by on-line computer processing of selected input data. An isokinetic sample of the off-gas stream is drawn through the filter/gas sample bottle array and the aerosol sample canister. The bank of five lines containing filters and gas sample bottles is operated in sequence to collect particulates and gas samples at different times during power operation. Following each MCCI test, gas sample bottles are removed for gas mass spectrometer analysis, filters are removed to determine the mass of aerosol collected, and coupons exposed to the main or sample gas streams are removed for scanning electron microscope (SEM) evaluation.

Additional details of the test equipment and procedures are described in Ref. 6.

MCCI TEST RESULTS

Interaction of a fully oxidized core melt with a limestone/common sand basemat has been simulated in three MCCI tests. The tests differed in the power input sequence and the capabilities of the aerosol collection and gas sampling system.

For MCCI test I-5, the test apparatus contained a 30.5-cm deep concrete basemat weighing 31 kg and a 21 kg inventory of fully oxidized corium containing eight grams of La_2O_3 to simulate nonvolatile fission products. A transfer to the high-power mode of operation was made after a preheat of 95 minutes. Power input was held steady at 10 kW and an argon carrier gas flowrate of 40 ℓ/m established in the gas system. A gas sample was collected at 10 kW, then the power was increased in five kW steps about every 15 minutes in a step-and-hold manner. Gas samples were also collected at 20 kW and 30 kW.

Ablation of concrete, production of decomposition gases, and transport of aerosols were observed in MCCI test I-5. Gases produced by the MCCI reached the gas system through eructations above the initial corium surface, then through the void following collapse of the corium overlayer. Molten material that was transported upward through the eructations contacted the top cover and dropped back onto the corium surface as globules. Temperature traces from Type-K thermocouples imbedded in the concrete exhibited an accelerating temperature increase followed by a sharp ramp to failure as the molten corium approached each thermocouple junction, as illustrated in Fig. 3 for MCCI test I-5. Additional detail on MCCI test I-5 is contained in Ref. 6.

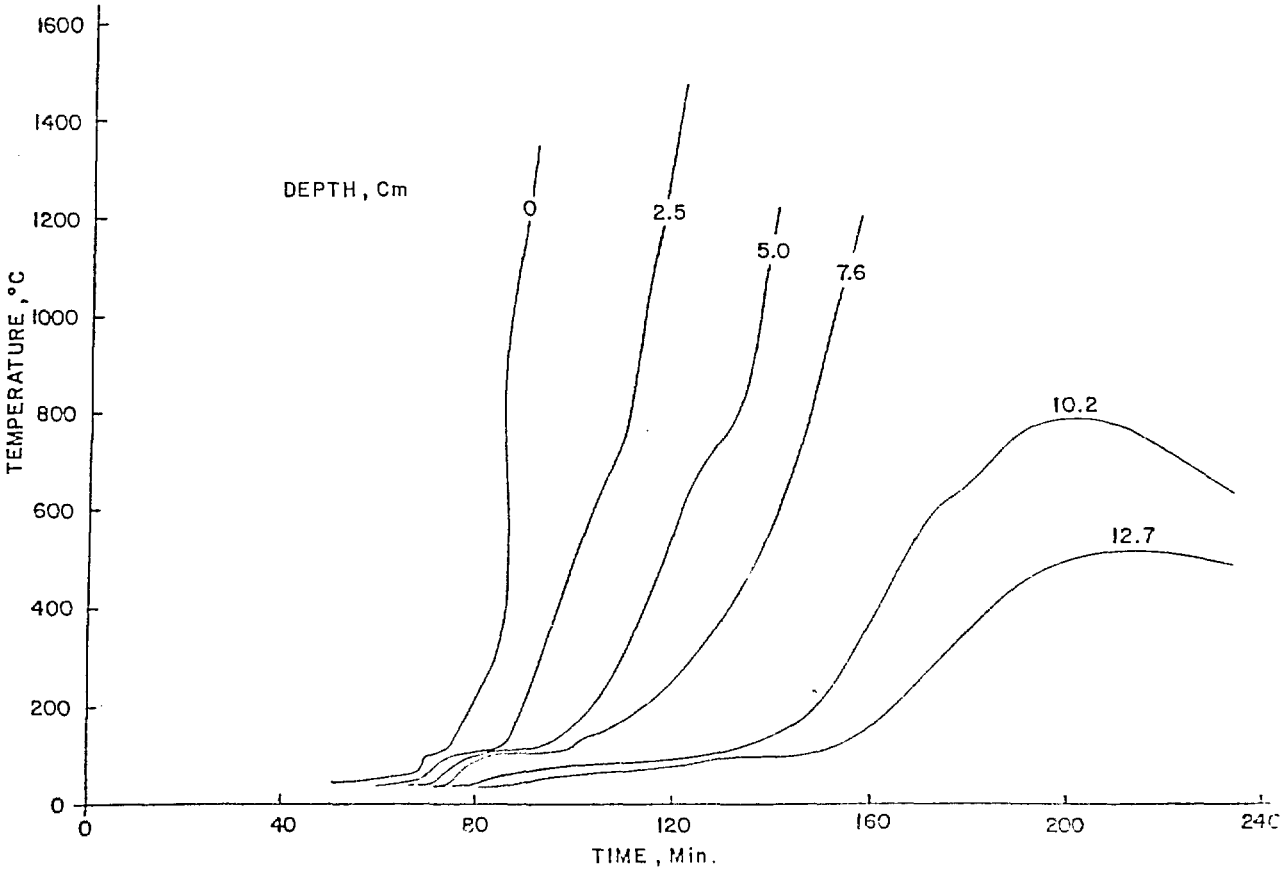

Figure 3. Response of Thermocouples in the Concrete Basemat During MCCI Test I-5

The event sequence and material response during MCCI tests I-6 and I-7 were similar to that described above for test I-5. In MCCI test I-7, sample gas flow was established through a filter and gas sample line coincident with the transfer to high power at 41 minutes. Sampling through this line continued until immediately prior to contact of the molten corium with the concrete surface. The first gas sample was collected. Gas sample flow was initiated in filter/gas bottle line 2, coincident with establishing sample flow through the STEP canister. Sampling intervals for the last four filter/gas bottle lines was about 10 minutes; sample flow was maintained through the STEP canister for 30 minutes.

Parameters for MCCI tests I-5, I-6, and I-7 are summarized in Table 2. The MCCI tests were limited by electrode size to a maximum ablation depth of

TABLE 2. CORIUM INVENTORY AND MELT LAYER CHARACTERISTICS IN INTERMEDIATE-SCALE MCCI TESTS

	Test		
	I-5	I-6	I-7
Corium inventory, kg	21	27	28.8
"Fission products," g	8 La_2O_3	42 BaO 42 La_2O_3 24 SrO	45 BaO 45 La_2O_3 26 SrO
Preheat, min	95	54	41
High power, min	82	60	90
Depth of concrete ablation, cm	7.6	~ 7	~ 7.5
Melt layer thickness, cm	4.6	~ 2.5	~ 5.5
Density of melt layer, g/cm^3	4.1	4.2	~ 4.2

~ 7.6 cm. The interface between the concrete and the melt, shown in Fig. 4 for MCCI test I-5, was smooth and flat. This was typical of the interface in all the MCCI tests. The density of the melt layer in MCCI tests was only 60% of that in the earlier gas sparge tests, indicating that concrete constituents were incorporated in the melt. Small-diameter gas passages penetrated the melt layer to the concrete surface. About 23%, or 7.3 kg, of the concrete basemat was ablated during MCCI test I-6.

The rate of concrete ablation was sensitive to test power input. Ablation rates determined from the in-concrete thermocouple responses are shown in

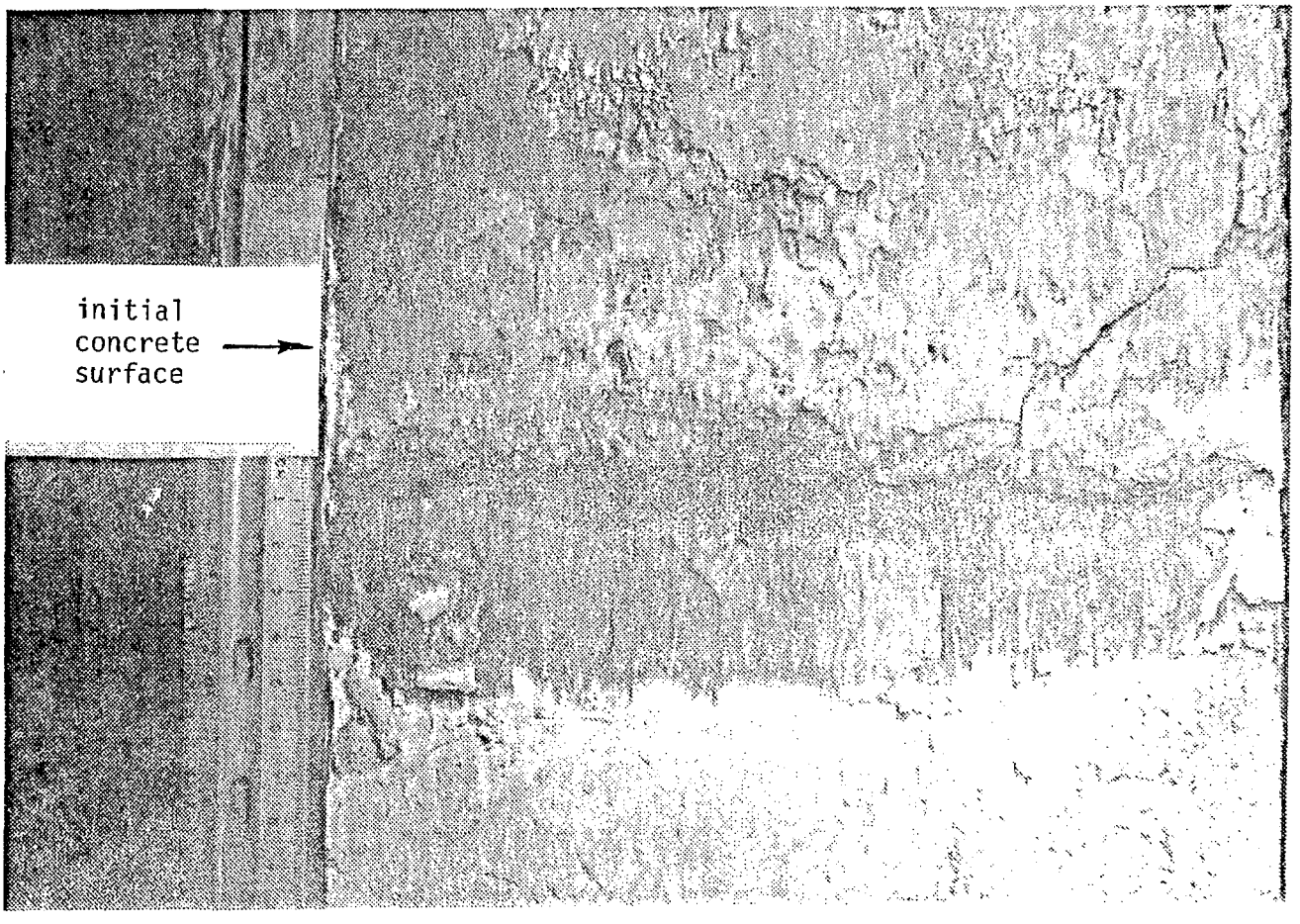

Figure 4. Interface between Concrete and Melt Layer in MCCI Test I-5.

Fig. 5. They vary from a maximum of 3.9 mm/min in tests I-6 and I-7 to a minimum of about 0.9 mm/min. The ablation distance as a function of time for test I-7 as calculated by the code CORCON[7] is also shown in Fig. 5. These calculations are discussed in the following section.

Borosilicate glass filters located in the main gas line and the sample gas lines had a minimum retention efficiency of 93% for 0.1 μm particles and collected aerosols principally by impaction. Table 3 lists the sampling interval and the mass of aerosol collected by each filter during test I-7. A total of 400 mg of aerosol was collected. The average aerosol transport during I-7 power operation was 4.5 mg/min. This rate did not remain fixed.

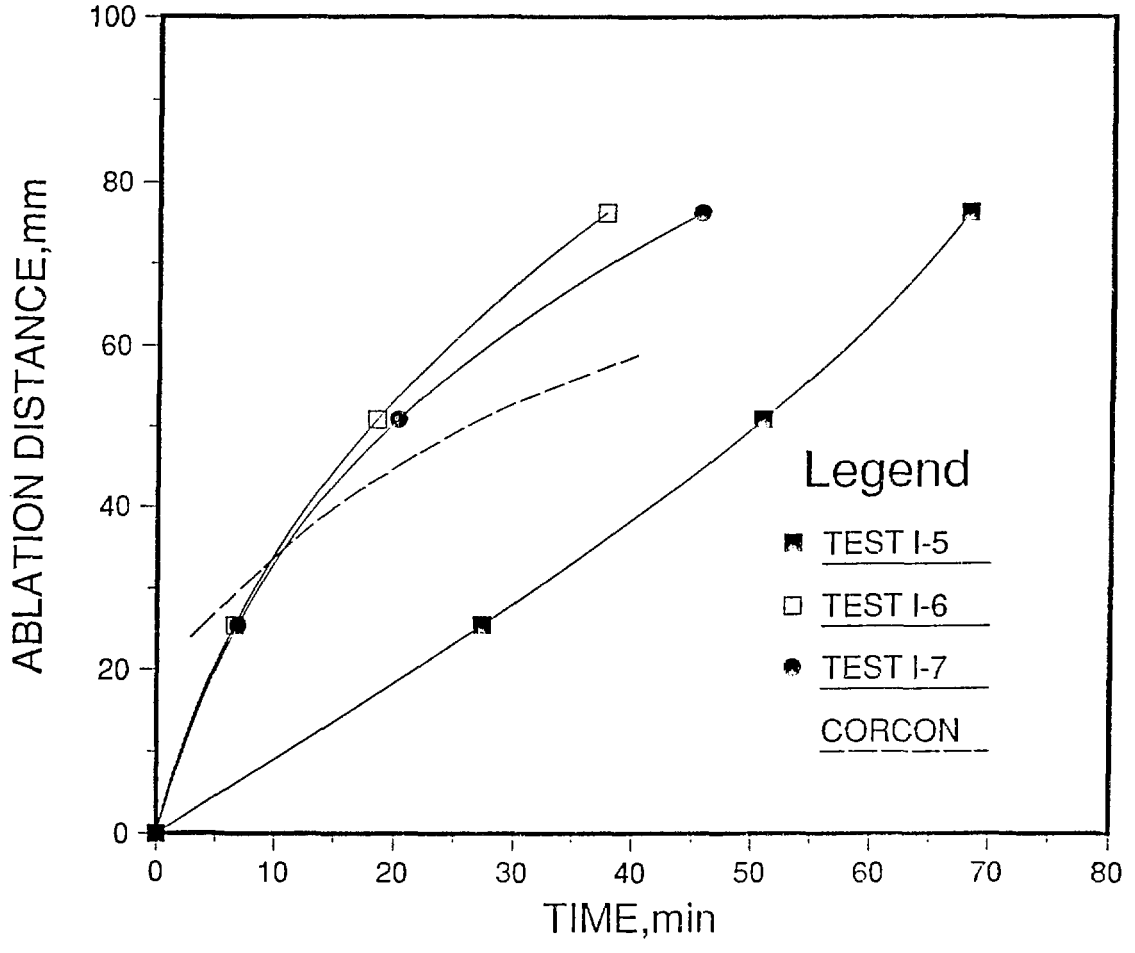

Figure 5. Ablation Distance vs. Time during MCCI Tests.

TABLE 3. MASS OF AEROSOL COLLECTED IN MCCI TEST I-7

Location	Mass Collected, mg	Time of Exposure, minutes
Main filters		
Filter 1 (south)	155.1	90
Filter 2 (north)	155.3	90
200 dpm α		
800-2000 cpm β-γ over background		
Filters in sample lines		
Line 1	3.6	39.1
Line 2	12.2	10.2
Line 3	4.2	9.8
Line 4	4.3	9.8
Line 5	4.9	10.0
STEP canister	11.2	29.8
Gas system liner (each section 51 in. long)		
Below lower sampling nozzle	12	90
Between lower and upper sampling nozzles	8	90
Above upper sampling nozzle	5	90

Data from the sample-line filters indicate that during the initial interaction of molten corium with the concrete the rate (10 min average) was three times higher than during subsequent sample intervals. The concentration of aerosol in the isokinetic sample during the 10-minute interval bounding initial corium concrete interaction was 0.37 mg/liter.

Peaks in the concentration of CO_2, CO, and moisture in the off-gas stream were also observed coincident with the initial contact of molten corium and concrete. The peak CO_2 concentration was 8%; corresponding peak concentration for moisture and CO were 1.5 and 0.09%, respectively.

Samples of melt material were taken from the top and bottom of the melt layer and from a surface eructation for chemical analysis. This material was characterized after dissolution using an inductively coupled plasma/atomic emission spectrometer (ICP/AES) to determine metals following ion-exchange separation of uranium to avoid spectral interference. Uranium was determined using a fluorescence technique. Variations were found in the composition of the melt material, particularly between the top and the bottom of the melt layer. Results of the spectrochemical analysis of the melt material at the sample locations in MCCI test I-7 are compared with the initial corium powder composition in Table 4. Table 4 also contains the SOLGASMIX[8]-calculated composition of the melt at 2600 K; these calculations are described in the next section. The components of stainless steel and the nonvolatile fission product simulants remained uniformly distributed. Uranium and zirconium had a higher concentration in the bottom of the melt layer than elsewhere. The insoluble residue contained chromium and iron in major amounts, with a minor amount of nickel. Lumping the residue weight fraction with that of the corium constituents, the concrete-based constituents, which are the lowest density materials present, were 4.5 w/o of the melt material at the bottom of the melt layer, but 30 w/o of the melt at the top of the melt layer and in the eructation.

Aerosol Sampling and Analysis

Aerosols released during the MCCI tests were collected by gravitational settling, impaction, interception, and diffusion. In test I-5, sets of four stainless steel coupons were positioned at two elevations in the gas system and exposed to the off-gas flow stream for the entire test. The upward facing coupons collected particles by gravitational settling and diffusion; downward facing coupons collected particles by impaction, interception, and diffusion.

TABLE 4. MAJOR CONSTITUENTS IN MCCI TEST I-7 CORIUM AND THE MELT MATERIAL*

Constituent	Composition, w/o				
	Pretest Corium Powder	Eructation	Melt Layer Top	Melt Layer Bottom	Calculated (2600K)
UO_2	54.3	32.7	36.9	49.6	44.2
ZrO_2	14.4	10.9	10.6	15.7	15.4
Cr_2O_3	5.7	1.0	0.5	1.1	5.9
NiO	2.2	1.6	1.5	1.4	1.3
Fe_2O_3	23.0	18.1	17.0	16.2	24.5
La_2O_3	0.16	0.11	0.11	0.10	0.18
BaO	0.16	0.12	0.12	0.11	0.17
SrO	0.09	0.07	0.07	0.07	0.11
CaO		9.2	9.0	1.1	2.8
MgO		4.0	3.8	0.35	0.92
Mn_2O_3		0.08	0.08	0.06	0.00
SiO_2**		18.0	15.1	3.1	4.4
insoluble residue		4.19	5.3	11.17	-

*an oxide form assumed for all constituents
**estimated by difference

In tests I-6 and I-7, the STEP canister was the principal aerosol sampling device and was open to sample gas flow for part of the power operation. Settling plates in the STEP canister collected particles by gravitational settling and diffusion; the fine wires collected particles by impaction, interception, and diffusion. The coupons, settling plates, and wires were examined by SEM to determine particle size, shape, extent of agglomeration, and elemental composition for atomic numbers > 13.

In MCCI test I-5, particles collected on the downward facing coupons by impaction and interception consisted of submicron spherical particles and irregular, stringy agglomerates composed of submicron particles. The

particles ranged from 0.1 to 1 μm in diameter with 0.4 μm as the average. The deposits on gravitational settling coupons (facing upward) consisted of large particles and large rounded agglomerates 2 to 3 μm in diameter. These agglomerates frequently contained a large particle upon which submicron particles had nucleated.

The wire impactors in MCCI test I-7 had three particle populations: 2-6 μm spheres, submicron particles, and irregular agglomerates. Figure 6 shows a platinum wire from the last stage of the STEP canister with these three particle populations. 2-6 μm spheres were also detected on the settling plates but not in as great a concentration as that on the wires. In addition, the deposits on the settling plates contained significant numbers of submicron particles and some larger particles and agglomerates. Submicron particle nucleation on larger particles and spheres was observed, as in test I-5. The average diameter of the larger particles and agglomerates varied from 3 to 13 μm with an average of 8 μm. A typical agglomerate is shown in Fig. 7.

The settling velocities for various particle sizes were determined using Newton's resistance law for the force resisting the motion of a sphere through a gas.[9] Newton's law of resistance is used to determine the settling velocities rather than Stoke's law because the Reynolds number for the gas system is 1600. Newton's law applies for Re > 1000; Stoke's law for Re < 1. Calculations of settling velocities for spheres with diameters from 2-6 μm and densities in the range 2.6-7.3 g/cm^3 in a mixture of steam, CO, and CO_2 at ~ 500 K and in argon at 373 K give settling velocities that range from 0.32 cm/s to 3.45 cm/s. In addition, calculations were performed for irregular particles using equivalent diameters of spheres in the 8-13 μm range and densities from 2.6-5 g/cm^3. The settling velocities for these irregular particles range from 1 to 4 cm/s.

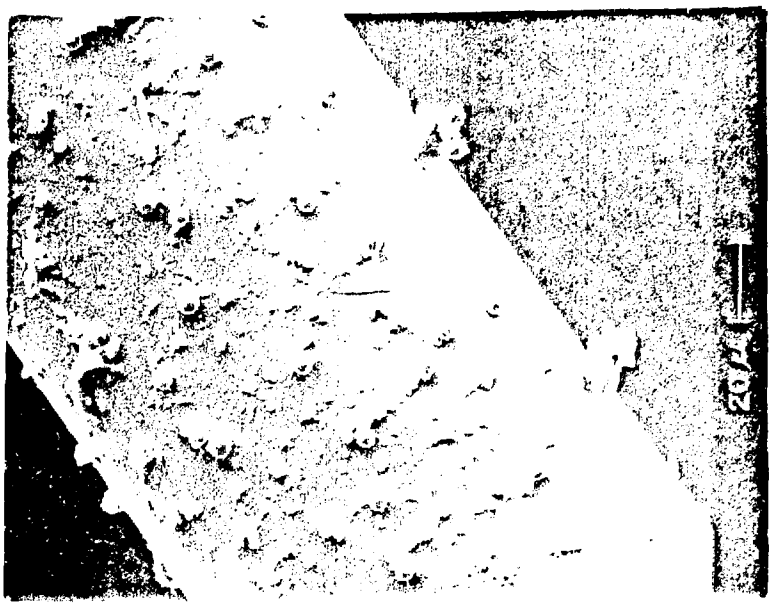

Figure 6. A Platinum Wire from Stage 14 (the last stage) in the STEP Canister Chamber Showing Deposits of Submicron Particles, Irregularly Shaped Agglomerates, and a Number of Spheres.

Figure 7. This Agglomerate from a Stainless Steel Settling Plate in Stage 7 is Composed of Silicon, Calcium and Aluminum with Small Amounts of Chlorine, Iron, and Titanium.

The gas velocity in MCCI test I-7 through the eructation is estimated to be 61 cm/s. Thus, these particles could easily be carried from the melt through this opening by the escaping gas. Gas velocities through the injector region and the main gas line are about 40 cm/s and 65 cm/s, respectively, well above the settling velocities of these large particles and spheres.

Aerosol deposits were examined by SEM for elemental composition. For the most part, either large particles or agglomerates were examined to minimize the interference of the spectra from plates and/or mounts. Area scans were also performed over sections of wires and plates to determine the dominant elements released. The results of these area scans appear to be consistent with the large particle and agglomerate examinations.

SEM examination of test I-5 coupon B-1 (lower sample elevation, upward facing coupon), which collected material by gravitational settling, indicated that the deposits consist predominantly of zirconium with smaller amounts of chlorine and a trace of potassium. The deposits on the impaction coupon B-2 (lower sample elevation, downward facing coupon), also from test I-5, contained chlorine, potassium, silicon, and possibly some zirconium.

A number of deposits from the MCCI test I-7 were also examined by SEM. The dominant elements detected include uranium, iron, silicon, calcium, potassium, and chlorine with smaller amounts of chromium, aluminum, magnesium, and nickel. Barium was detected in one particle. Uranium was only found in spheres; almost all the 2-6 μm spheres contained uranium. Spheres on settling plates and wires were composed of uranium, silicon, and calcium, sometimes with smaller amounts of iron. Spheres similar to the one in Fig. 8 that are composed of uranium and iron, sometimes with small amounts of calcium and chromium, were found only on wires. The spherical shape indicates that the material comprising the spheres was molten. A number of crystalline deposits

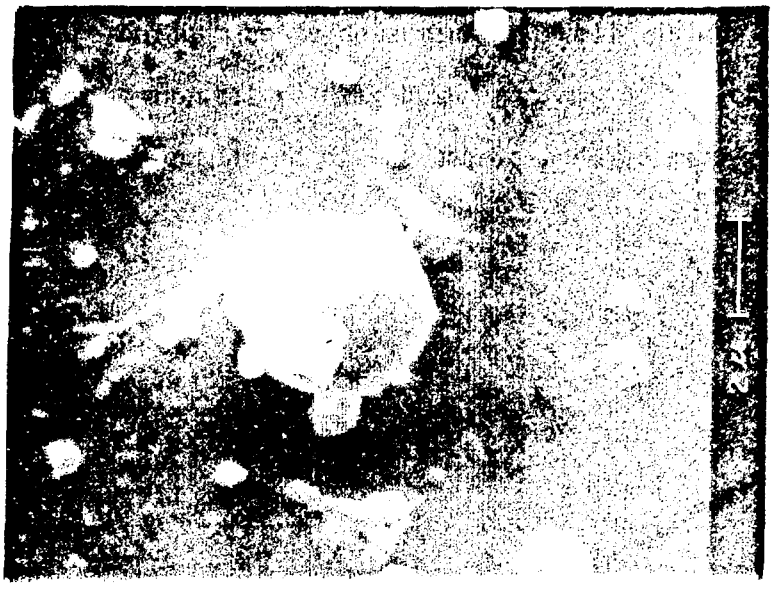

Figure 8. This Sphere Containing Uranium and Iron Has Served as a Nucleation Site for Smaller Aerosol Particles. It is Located on a Gold Wire in the First Stage of the STEP Canister Chamber.

was detected on wires and settling plates. Cubic crystals composed of potassium and chlorine, which are most likely potassium chloride, were frequently observed. Often these crystals comprised part of a larger agglomerate. A number of large particles contained silicon, and/or calcium and magnesium. These may have been particulate from the concrete that was transported by mechanical entrainment. No lanthanum or strontium was detected in any aerosols from MCCI tests. In test I-7, no zirconium was detected but uranium was dominant in the spheres whereas in test I-5, zirconium was frequently found in gravitational settling deposits but no uranium was detected. In both tests, silicon, potassium, and chlorine were found. An SEM examination of the main filter revealed a heavy surface loading of aerosol.

Calculations are being made to determine how well various computer models characterize these experimental results both in terms of the chemical constituents of the aerosols released and of the debris bed and also in terms of the

ablation of the concrete. Comparisons are planned with the computer codes CORCON,[7] SOLGASMIX,[8] and VANESA.[10]

The CORCON-calculated ablation distance as a function of time for MCCI test I-7 is shown in Fig. 5. CORCON calculated a peak ablation rate of 1.45 mm/min, decreasing to 0.53 mm/min by 40 minutes. The CORCON model does a heat balance of power into the melt, heat loss to the sides, radiation loss above the melt, and determines the melt temperature, the heat flux into the concrete, and the ablation rate. In MCCI test I-7, the sintered corium overlayer acted as a heat shield to radiation loss from the melt surface. The radiation heat loss is estimated to be reduced by 20% by the presence of a heat shield with an emissivity similar to that of UO_2. No provision for an axial heat shield exists in the CORCON model. Thus, the melt temperature, heat flux into the concrete, and the ablation rate would be greater than the values predicted by this CORCON calculation.

Calculations using SOLGASMIX have been performed at 1800, 2000, 2200, 2400, and 2600 K for the material inventories and geometry of test I-7, using a 16-element and a 123-compound data base. Included in the data base are the elements and the oxides, hydroxides, silicates, and carbides of oxygen, hydrogen, carbon, silicon, calcium, magnesium, uranium, zirconium, lanthanum, barium, strontium, iron, nickel, chromium, aluminum, and helium. If the release of the gases from the concrete (O_2, CO_2, CO, H_2O, and H_2) is not included, the order of the vapor pressure of the gaseous species and thus the order of their release via vaporization at 2600 K is:

$AlOH > UO_3 > Ni > CrO_2 > FeO > Al_2 > Fe > SiO > CrO_3 > CrO > UO_2 > BaO$.

In the temperature range 2000 to 2400 K the order is similar except that BaO is more volatile than SiO. These calculations indicate that at 1800 K the partial pressure due to BaO would be greater than that for FeO. The vapor

pressures of the gaseous compounds of Mg and Ca are one order of magnitude below the vapor pressure of BaO. Thus, chemical-equilibrium calculations imply that more barium would be released than calcium or magnesium under the conditions of MCCI test I-7. However, SEM examination of aerosols from MCCI test I-7 indicates that calcium is one of the dominant elements in the aerosol deposits and magnesium is more prevalent than barium. Some of the aerosol particles that contain magnesium and/or calcium could be concrete particulates carried from the melt by mechanical entrainment, but the spheres that contain uranium and calcium are aerosols formed from the corium-concrete melt. Although the relative release of barium, calcium, and magnesium is not in agreement with results of chemical-equilibrium calculations, the dominance of uranium and iron and the small release of barium relative to uranium, iron, nickel, chromium, and silicon is in accord with chemical-equilibrium calculations. In addition, the equilibrium calculations indicate that the vapor pressure of oxides and hydroxides of strontium and lanthanum are on the order of 10^{-6} or lower; therefore strontium and lanthanum should not be detected. The calculations also indicate that no zirconium would be vaporized. No strontium, lanthanum, or zirconium were detected in the aerosol deposits from MCCI test I-7.

In addition to calculating the species vaporized, SOLGASMIX also determines the phases and chemical forms of the condensed species. If these are expressed in terms of the oxides of the solidified corium-concrete melt, they may be compared with the chemical analysis of the top and bottom of the melt. The calculated composition for a 2600 K melt is given in the last column of Table 4. For most constituents, the calculated weight fraction lies between those shown for the top and bottom of the melt. However, the calculated weight fractions of calcia and silica appear to be low. Recall that the

calculated vaporization of calcium and silicon species was also low, indicating that more calcium and silicon are present in the corium-concrete melt than the amounts determined by assuming uniform dissolution of the concrete constituents. Examination of the concrete-corium interface following the experiment indicated fingering. This may imply that harder aggregates containing denser material such as iron and chromium oxide may reside in the concrete whereas lighter more porous materials such as calcium silicate react with the melt.

FUTURE WORK

Each test has been conducted to generate a maximum amount of information as well as to serve as a test bed for further system development. Potential areas for improved aerosol collection and gas sampling and for improved measurement of corium melt temperature were identified as a result of the MCCI testing. Design changes that are being made in the aerosol collection and gas sampling system include the addition of

1. a pump in the main gas line to ensure transport of the decomposition gases and aerosols through the gas system,
2. an orifice meter to monitor the gas flow rate in the main system piping, and
3. a gas mass spectrometer for continuous, on-line analysis of the off-gas composition.

For measurement of corium temperature, additional high-temperature thermocouples are being located in thermowells imbedded in the concrete basemat.

Following upgrade of the test system, a pair of MCCI tests is planned. One test will be performed with fully oxidized corium; the corium inventory for the other test will contain unoxidized metal. The test results will identify the effect of metallics on the event sequence, gas composition and gas release rates, and the quantity and nature of aerosols produced during a MCCI.

Acknowledgement

The authors appreciate the assistance of J. Norkus, University of Wisconsin (Madison), for performing the CORCON calculations, R. Aeschlimann and R. Wesel for test preparations and operation, and V. Eustace for manuscript preparation.

References

1. D. Ross, M. Ernst, and J. Murphy, "NUREG-1150 Status Report: Current Perspectives on Nuclear Power Plant Risks and the Use of Risk-based Information in Regulation," Proc of The EPZ and the Source Term, An EPRI Information Meeting, Brookhaven National Laboratory, June 1-3, 1986.

2. D. Cubicciotti and B. R. Sehgal, "Fission Product and Material Vapor Transport During Molten Corium-Concrete Interactions," Proc Fifth Intl Mtg on Thermal Nuclear Reactor Safety, Karlsruhe, W. Ger, Sept 9-13, 1984, KfK 3880/3, Dec 1984.

3. J. J. Sienicki and B. W. Spencer, "Debris Dispersal in Reactor-Material Experiments on Corium-Water Thermal Interactions in Ex-vessel Geometry," Proc AIChE Symposium Series, 236, V. 80, 22nd National Heat Transfer Conf., Niagara Falls, NY, August 6-8, 1984.

4. J. J. Sienicki and B. W. Spencer, "The Jet Impingement Stage of Molten Core-Concrete Interactions," OECD CSNI Specialist Meeting on Core Debris/ Concrete Interactions, Palo Alto, CA, September 3-5, 1986.

5. B. J. Schlenger, P. F.Dunn, and E. L. Horton, "Versatile Aerosol Sampling System Developed for Nuclear Reactor Safety Experiments," (accepted for publication in Particulate Science and Technology).

6. B. W. Spencer, W. H. Gunther, D. R. Armstrong, D. H. Thompson, M. G. Chasanov, and B. R. Sehgal, "EPRI/ANL Investigations of MCCI Phenomena and Aerosol Release," OECD CSNI Specialist Meeting on Core Debris/Concrete Interactions, Palo Alto, CA, September 3-5, 1986.

7. R. K. Cole, Jr., D. P. Kelly, and M. A. Ellis, "CORCON-Mod2: A Computer Program for Anaysis of Molten-Core Concrete Interactions," NUREG/CR-3920; SAND84-1246 (August 1984).

8. Gunnar Erickson, Chemica Scripta, 8, 100-103 (1975).

9. W. C. Hinds, Aerosol Technology, J. Wiley and Sons Inc., New York, NY (1982).

10. D. A. Powers, J. E. Brockmann, and A. W. Shiver, "VANESA: A Mechanistic Model of Radionuclide Release and Aerosol Generation During Core Debris Interactions with Concrete," NUREG/CR-4308; SAND85-1370 (July 1986).